energies

MDPI

Article

High Hydrogen Evolution Reaction (HER) and Hydrogen Oxidation Reaction (HOR) Activity Rh_xS_y Catalyst Synthesized with Na_2S for Hydrogen-Bromine Fuel Cell

Yuanchao Li and Trung Van Nguyen *

Chemical and Petroleum Engineering Department of University of Kansas, University of Kansas, Lawrence, KS 66045, USA; yuanchao.li@ku.edu

* Correspondence: cptvn@ku.edu

Received: 17 June 2020; Accepted: 27 July 2020; Published: 2 August 2020

Abstract: A Rh_xS_y/C catalyst with high mass-specific electrochemical surface area (ECSA/mass), high hydrogen oxidation reaction (HOR)/hydrogen evolution reaction (HER) activity, and high Nafion® ionomer-affinity was synthesized and evaluated. A new sulfur source, Na_2S instead of $(NH_4)_2S_2O_3$, was applied to prepare the rhodium sulfide precursor Rh_2S_3 that resulted in a Rh_xS_y catalyst with higher HOR/HER catalytic activity after thermal treatment. The higher activity was attributed to the higher quantity formation of the more active phase Rh_3S_4, in addition to the other active $Rh_{17}S_{15}$ phase, in the Rh_xS_y catalyst. Using this new sulfur source, carbon substrate functionalization, and the mass-transfer-controlled nanoparticle growth process, the average particle size of this catalyst was reduced from 13.5 nm to 3.2 nm, and its ECSA/mass was increased from 9.3 m^2/g-Rh to 43.0 m^2/g-Rh. Finally, by applying the Baeyer–Villiger and ester hydrolysis process to convert the Nafion® ionomer-unfriendly ketone group on the carbon support surface to the Nafion ionomer-friendly carboxylic group, which increases the Nafion® affinity of this catalyst, its use in the hydrogen electrode of an H_2-Br_2 fuel cell resulted in a performance that is 2.5× higher than that of the fuel cell with a commercial Rh_xS_y catalyst.

Keywords: hydrogen-bromine fuel cell; rhodium sulfide catalyst; hydrogen evolution; hydrogen oxidation catalyst

1. Introduction

Sustainable and environmentally benign energy sources such as wind and solar are gaining more market penetration worldwide as they become more economically competitive against high CO_2 emission fossil fuel sources, such as coal [1–4]. However, the contributions of these renewable energy sources are still limited by their intermittent and unpredictable nature [4], which can create a challenge to the stability of the electrical network when they are integrated into the grid in large proportion. One of the methods to stabilize the electricity network and enable higher contributions from the wind and solar sources is to incorporate grid-scale storage technologies [5,6].

The H_2-Br_2 regenerative fuel cell is a hybrid fuel cell consisting of a gas-phase negative electrode of a fuel cell and an aqueous-phase positive electrode of a flow battery. After its first introduction in 1964 [7], it has gained great interest from the energy storage industry and academic institutions due to the fast kinetics of its electrode reactions and low-cost energy storage electroactive materials [8–11]. An H_2-Br_2 fuel cell involves an H_2 negative electrode, a Br_2 positive electrode, and a proton exchange membrane (PEM) as the electrolyte. The initial electroactive material of an H_2-Br_2 fuel cell is the HBr solution. During the charge mode, the bromide anions are converted to the neutral bromine

molecules at the positive electrode using excess electricity from an intermittent energy source like wind/solar. Simultaneously, the hydronium cations in the hydrobromide solution migrate across the PEM to the hydrogen electrode and are reduced to H_2. This process converts the electrical energy in the electricity to chemical energy in the form of hydrogen and bromine molecules while maintaining electroneutrality condition on both sides of the fuel cell. The HBr-Br_2/H_2 are stored externally in two separate storage tanks. When there is a demand for electricity from the electric grid, the electrical energy stored in the bromine and hydrogen molecules is released when the electrochemical reactions and proton transport process across the membrane described earlier are reversed, in its discharge mode, converting hydrogen and bromine back to HBr. The low price of the starting material, HBr, is one of the main advantages of the H_2-Br_2 system. Currently, the bulk price of HBr is about $2/kg in comparison to $15/kg for vanadium, the electroactive material used in the commercialized all-vanadium flow battery system [12,13].

The fast kinetics of the bromine/bromide reaction on non-precious materials, such as carbon, is another advantage of the H_2-Br_2 fuel cell. However, the hydrogen oxidation reaction (HOR) and hydrogen evolution reaction (HER) at the negative electrode requires a precious metal catalyst. The application of a hydronium-cation-selective membrane, such as Nafion®, cannot completely prevent the crossover of the bromide anion and bromine molecules from the HBr side to the hydrogen side. Earlier durability studies of the H_2-Br_2 fuel cell show that the commonly used Pt catalyst for the hydrogen reactions is vulnerable to corrosion and poisoning by Br^-/Br_2 [14–16]. The main challenge to the deployment of the H_2-Br_2 system has been the availability of a durable and high-activity electrocatalyst for the hydrogen reactions. The current research of HOR/HER catalyst in H_2-Br_2 fuel cells can be grouped into two main efforts, one for more durable catalysts and the other to protect the Pt catalyst. Pt-Ir-N_x/C [17] and MoS_2-Pt [18] have been investigated and found to be almost as active and a bit more durable than Pt in the HBr/Br_2 solution. However, their stability still does not meet the long-term (10–20 years) durability requirement for these electrochemical energy storage systems. In the efforts on protecting the Pt catalyst, the polydopamine coating on Pt was found to provide some protection of the metal from the corrosion by bromine/bromide. The impact of the polymer coating on the hydrogen reaction rate is an issue that must be addressed [19,20]. Our previous studies suggest that the active Rh_xS_y phases are suitable catalyst candidates for the HOR/HER in the Br^-/Br_2 solution because they show reasonable catalytic activity for the HOR/HER and outstanding stability in this corrosive environment [21–23].

The current commercially available Rh_xS_y catalyst has two issues, low mass-specific electrochemical active surface area (ECSA) and low catalytic activity [22]. The functionalization of the carbon support and the employment of the mass-transfer-controlled nanoparticle (NP) growth process resolve the low mass-specific ECSA caused by the large and broad distribution of NP size. Using these approaches, the Rh_xS_y catalyst nanoparticle size was reduced from ~13 nm to ~5 nm [24,25]. The low HOR/HER activity of the current Rh_xS_y catalyst is related to the composition of the crystal phases in the catalyst. There are three rhodium sulfide crystal phases, Rh_2S_3, Rh_3S_4, and $Rh_{17}S_{15}$ [26–28]. Among these crystal structures, Rh_2S_3 is a semiconductor and has no catalytic activity while Rh_3S_4 and $Rh_{17}S_{15}$ show high catalytic activity for the HOR/HER. Their mixtures are often called Rh_xS_y. The non-active Rh_2S_3 phase can be converted to Rh_3S_4 and $Rh_{17}S_{15}$ by thermal treatment during which some sulfur atoms are removed from the Rh_2S_3 structure. In addition to the aqueous method of synthesizing Rh_2S_3 and converting it to Rh_3S_4 and $Rh_{17}S_{15}$ by thermal treatment used in our approach, the gas-phase process of direct sulfidation reaction of $RhCl_3$ and gaseous H_2S, used by others, also results in the mixture of multiple rhodium sulfide phases where the phase composition is determined by the synthesis temperature, temperature ramp rate, and treatment time [26]. The density functional theory (DFT) calculation suggests that the Rh_3S_4 crystal phase has the highest HOR/HER activity [27].

The substitution doping with other metal atoms has also been explored as a method to improve the intrinsic activity of rhodium sulfide. Prior doping attempts, however, show that rhodium sulfides incorporated with Ru and Pd did not show higher HOR activity [28]. As an alternative approach to

resolve the low-activity issue, we focus our efforts on the adjustment of the crystal composition of rhodium sulfide. To adjust the crystal composition of rhodium sulfide, we explored the two methods of tuning the thermal treatment temperature and exploring the new types of sulfur sources. The narrow free energy window among these three rhodium sulfide crystal phases [29,30] shows the challenge one faces in this conversion process. If the treatment temperature is either too low or too high, one may end up with either too much of the unconverted non-active Rh_2S_3 phase or Rh metal. Rhodium metal is an unwanted phase because it is unstable in HBr/Br_2 like platinum [23,31]. A recent study has shown that different sulfur sources can lead to different metal sulfide monomers (building blocks of nanoparticles) and final compositions. For example, the synthesis of nickel sulfide with sodium thiosulfate and C_2H_5NS under the same experimental conditions yield Ni_3S_4 and NiS, respectively [32].

In this study, Na_2S was evaluated as an alternative sulfur source for synthesizing rhodium sulfide catalyst that contains a higher level of the more active Rh_3S_4 phase, instead of the ammonium thiosulfate source used in our previous studies and in the synthesis of some commercial rhodium sulfide catalysts [22–25,33–35]. To the authors' best knowledge, this is the first reported work to use different sulfur sources to adjust the crystal phases of Rh_xS_y. Cyclic voltammetry (CV) was used to determine the increase in the mass-specific surface area of the rhodium sulfide catalysts synthesized with the functionalized carbon substrate and the diffusion-controlled nanoparticle growth process, and to prove that the rhodium sulfide catalyst synthesized by Na_2S had a higher HOR activity. The higher HOR activity of the catalyst will also be validated by the linear polarization curves obtained by the multiple-step chronoamperometry. Transmission electron microscopy (TEM) was used to confirm the decrease in the average particle size of nanoparticles. X-ray Photoelectron Spectroscopy (XPS) was the main method used to confirm the surface elemental composition of the crystal phase that was responsible for the increase in the activity of the Rh_xS_y catalyst synthesized with Na_2S. The H_2-Br_2 fuel cell tests were the final validations used to compare the performance of the rhodium sulfide catalyst on functionalized carbon support synthesized with Na_2S to those of the rhodium sulfide catalyst synthesized with ammonium thiosulfate and the commercial rhodium sulfide.

2. Materials and Methods

2.1. Functionalization of Carbon Substrate

The carbon substrate was functionalized by the previously reported method [25]. The activated carbon, XC72R, was functionalized by three steps: Oxidation in the 70% *w*/*w* HNO_3 solution, reduction in H_2 at 300 °C, and overnight air exposure at room temperature. The three-step functionalization was used to create a widely distributed ketone-dominated carbon surface that would be needed to attract the rhodium cations and precipitate the rhodium sulfide precursor Rh_3S_4 phase uniformely on the carbon support surface [25]. The application of these processes is expected to create nanoparticles that are smaller and more dispersed.

2.2. Synthesis of Rhodium Sulfide Catalyst

In the first step of this process, $RhCl_3{\cdot}3H_2O$ was dissociated in DI water and refluxed at 100 °C for 2 h. Next, the functionalized carbon powder dominated with ketone groups on the surface was added to the solution with the weight ratio of Rh to C of a 1:3. The solution was then sonicated for 2-h to disperse the solid. $Na_2S{\cdot}9H_2O$ was dissolved in DI water by the weight ratio of water to sulfide ion of 6.84:1 (sulfide molar concentration is around 4.5 M). To create a diffusion-controlled NPs growth process, the sodium sulfide solution was added to the $RhCl_3$/carbon mixture at 100 °C at the rate of 3 mL/h by a peristaltic pump. The S^{2-} anion from the dissociated Na_2S precipitated Rh^{3+} on the pretreated carbon. The precursor material, Rh_2S_3/C, was centrifuged and washed by DI water and dried at 90 °C overnight. The thermal treatment converted the inactive Rh_2S_3 phase into the active Rh_3S_4 and $Rh_{17}S_{15}$ phases in a quartz tube reactor under continuous argon gas purge, during which

sulfur atoms were released. The thermal treatment was done at the previously reported temperature and temperature ramping rates [25].

In our previous study, the ketone groups on the carbon support surface needed in the catalyst synthesis were found to have low affinity to the Nafion® ionomer used as the solid electrolyte in the catalyst layer, and this led to poor fuel cell performance [25]. The Baeyer–Villiger reaction was used to convert the ketone groups on the carbon support to the more Nafion®-friendly carboxylic groups that resulted in a better and more uniform distribution of the Nafion® ionomer on the catalyst surface in the fuel cell catalyst layer [24]. In this conversion process, the rhodium sulfide catalyst powder and the Baeyer–Villiger reaction agent (9-Mesityl-10-methylacridinium perchlorate) were mixed by a weight ratio of 6.5:1. The mixture was then dissolved in methanol to about 1.82 mg/mL concentration. An amount of 0.5 mL of 30% H_2O_2 was added for every 100 mg of rhodium sulfide catalyst. The mixture was refluxed at 55 °C for three days. The solid was washed with DI water and centrifuged seven times and then dried overnight at 100 °C. The final product group on the carbon surface after the Baeyer–Villiger reaction treatment was the ester group that would then be converted to the carboxylic group by hydrolysis. In the hydrolysis step, 1 mg of the treated catalyst was mixed with 1 mL of 36% (*w*/*w*) HCl solution and refluxed at 77 °C for 8 h. The product was washed with DI water and centrifuged, and this process was repeated until the pH of the washing solution reached ~7. Finally, it was dried overnight in the air at 100 °C.

2.3. Characterizations

The morphology of the samples was determined by an FEI Tecnai F20 XT Field Emission Transmission Electron Microscope (TEM) at an acceleration voltage of 200 kV. X-ray powder patterns were obtained by using monochromated Cu-Kα radiation (λ = 1.54178 Å) on a Bruker Proteum diffraction system equipped with Helios high-brilliance multilayer optics. A Platinum 135 CCD detector and a Bruker Microstar microfocus rotating anode X-ray source were operated at 45 kV and 60 mA. The scanning was done from 10–90° (2θ) with a step size of 0.5°. In the XPS measurements, the prepared catalysts were analyzed by a PHI 5000 Versa Probe II electron spectrometer with monochromated Al as the X-ray source. The XPS binding energies were measured with a precision of 0.2 eV. The analyzer pass energy was set at 23.5 eV, the take-off angle was 45°, and the beam size was 100 microns. For each measurement, the XPS spectra were corrected to the internal reference spectra of C 1s at 284.5 eV to compensate for electrostatic charging.

2.4. Electrode Preparation

The electrode prepared here was used only for the cyclic voltammetry (CV) test rather than the fuel cell test. To provide a more accurate measurement of the loaded catalyst mass, a gas diffusion electrode (SGL-10AA) was used instead of the commonly used glassy carbon rotating electrode (GC-RDE) coated with the catalyst. The carbon paper was pretreated in 2 M HNO_3 solution to make it hydrophilic to make it easier for the electrolyte to penetrate into the electrode. The catalyst loading process can be found in our previous work [23–25,31].

2.5. Cyclic Voltammetry

All electrochemical measurements were made with a Gamry Potentiostats (Interface 1010E). The three-electrode system of cyclic voltammetry included a gas diffusion electrode (GDE) made in the above-mentioned procedure as the working electrode, a saturated calomel electrode (SCE) as the reference electrode, and a Pt wire as the counter electrode. The working electrode (GDE) was clamped by two graphite plates, which were connected to the potentiostat via an epoxy coated nickel wire. The reference electrode was placed adjacent to the working electrode. Details of the working electrode set-up can be found in our previous publications [23,31]. Unstirred nitrogen-saturated 1 M H_2SO_4 served as the electrolyte. All measurements were taken at room temperature (~22 °C) unless otherwise stated. The electrochemical active surface area (ECSA) of the catalyst was calculated in comparison to

platinum. The equation used to calculate the Pt equivalent ECSA was ECSA = Q_H / 0.21, where the Q_H was calculated from the integration of the current vs. time curve of the HOR peak with correction for double-layer charging, which is then divided by the 0.21 mC/cm^2 [36,37] value to determine the equivalent ECSA to that of Pt. This is done for comparison purpose since this material is developed as a replacement to Pt. That is, if the integrated HOR peak area is 0.21 mC, the ECSA of this catalyst is said to have an area with equivalent activity to 1 cm^2 of Pt. This allows the mass activity of all rhodium sulfide catalysts to be compared among themselves and to the Pt catalyst. Since the solution is an H_2-free solution, the source of the adsorbed H in the HOR process in the positive CV scan comes from the HER process (the negative current region of the CV). The intrinsic ECSA of the catalyst can be measured accurately by oxidizing only a monolayer of adsorbed H. The existence of gaseous H_2, generated during the HER process, near the catalyst surface could have some effect on the measured ECSA. However, since the same CV scan range was used in all measurements, this effect is expected to have the same impact on all catalyst types. For the activity comparison study conducted here, this effect is not expected to alter the conclusions made with the results. The voltage of the working electrode was repeatedly scanned from 0 V to 0.425 V vs. RHE for five cycles, and the results from the last cycle were used in the ECSA calculation.

2.6. Multiple-Step Chronoamperometry

The exchange current density (i_o) is used to evaluate the intrinsic electrochemical activity of a catalyst. In the kinetics-controlled region ($|\eta| < 25$ mV) which is almost free of ohmic and mass-transfer effect, the Butler-Volmer equation can be simplified to a linear relationship as,

$$i = i_o \frac{nF}{RT} \eta \tag{1}$$

where I is the measured current divided by the ECSA (or A/cm^2 of the active area), i_o is the exchange current density in A/cm^2 of the active area, F is Faraday's constant, R is the universal gas constant, T is the temperature in K, and η (=$E - E_{eq}$) is the overpotential. A 30 µL of the catalyst ink prepared similarly to the ink solution used in the CV measurement was dropped on the surface of a glassy carbon RDE followed by another 10 µL of 0.1% wt Nafion® solution on top of the catalyst. The RDE with the loaded mixture of catalyst and Nafion® ionomer was dried at 60 °C for 30 min in an oven and then cooled to RT. The ECSAs of the loaded catalyst before and after the activity test were measured by CV in an unstirred N_2-saturated 1 M H_2SO_4 solution. The ECSA of each catalyst was calculated by averaging the initial and final ECSA values. This is done to account for any potential loss of catalyst during the rotation of the electrode. After the initial ECSA measurement, the nitrogen purging was replaced by the hydrogen purging. The HOR/HER activity was measured with an RDE rotated at 2400 rpm. The activity calculation only uses the data in the kinetics-controlled region (linear region of i-E curve).

2.7. Fuel Cell Testing

Testing in an H_2-Br_2 fuel cell was used to evaluate the catalyst performance in its actual application. The positive (bromine) electrode was composed of three layers of 1 cm × 1 cm plain SGL carbon (10AA) gas diffusion layer (GDL) treated with 2 M HNO_3 solution to make it hydrophilic, while the negative (hydrogen) electrode was made of a bi-layer carbon gas diffusion medium (SGL 25BC) coated with a Rh_xS_y/C catalyst. The weight ratio of Rh_xS_y/C and Nafion® ionomer in the coated catalyst layer was about 1:1. A brush was used to paint the catalyst ink onto the microporous layer (MPL) side of the bi-layer carbon gas diffusion medium. The catalyst loading in the hydrogen electrode was approximately 2.3 mg/cm^2, where the mass is the total mass of the catalyst and the carbon support. The membrane electrode assembly (MEAs) wase made by hot pressing the catalyzed hydrogen electrode onto one side and placing the tri-layer of carbon electrode onto the other side of a commercial Nafion® 212 membrane. The same procedure was used to make the MEAs for all rhodium sulfide catalyst types.

The humidified H_2 gas was recirculated through the negative electrode at 122 kPa, while 13 cm^3/min of the 1 M HBr/0.9 M Br_2 electrolyte mixture was circulated through the positive electrode side of the H_2-Br_2 fuel cell. An excess HBr/Br_2 solution was used to ensure the Br_2/Br^- concentration remained constant during the polarization tests. Interdigitated flow fields were used on both sides of the fuel cell for all experiments [38]. The experiments were conducted at room temperature (~22 °C) unless otherwise specified. At the end of each experiment, an electrochemical impedance spectrum (with Gamry EIS 300, amplitude: 5 mV, and frequency range: 0.1 Hz to 100 kHz) of the cell was obtained, and the internal ohmic resistance of the fuel cell was acquired from the high frequency intersection of the impedance curve and the real impedance axis in a Nyquist plot.

3. Results

The Rh atoms in the crystal structures of Rh_xS_y can roughly be divided into two categories, Rh atoms bonded with neighboring Rh or neighboring S. The rhodium atoms coordinated with another Rh atom in the crystal structure have more metal characteristics and are the more catalytic active centers for the HOR. These active HOR sites are also active sites for the HER. The rhodium sites coordinated with sulfur atoms and the sulfur atoms are both active sites for the HER. The dual catalytic centers make the Rh_xS_y a bifunctional catalyst for the HER and HOR where the HER activity is higher than the HOR active because of the larger number of HER sites versus HOR sites. DFT studies show that the Rh_3S_4 phase should exhibit the highest HOR activity [27]. The different Rh-Rh bond energies in the crystal structures may explain the reason. The closest Rh-Rh bond lengths of metal Rh, Rh_2S_3, Rh_3S_4, and $Rh_{17}S_{15}$ measured by experiments are 2.73 Å [29], 3.20 Å [39], 2.70 Å [40], and 2.63 Å [29], respectively, among which the bond length of Rh_3S_4 is closest to that of metal Rh. The similarity between the bond lengths of Rh_3S_4 and Rh suggests that the HOR-active Rh centers of Rh_3S_4 have the most similar electronic density with those of metal Rh. The Pm3m space group of $Rh_{17}S_{15}$ contributes to a stronger Rh-Rh bond with a shorter length. The adsorption and desorption of reactant and product require an appropriate electron density of active sites based on the Hammer-Norskov model [41]. In this case, the higher electron density of the Rh centers in $Rh_{17}S_{15}$ may result in an over-strong adsorbate H-metal (Rh of $Rh_{17}S_{15}$) bond which could finally obstruct the removal of the product H^+ in the HOR. As described in Section 1, inappropriate treatment temperatures could lead to the formation of metal Rh or excessive inactive Rh_2S_3 phase, due to the narrow free energy window among Rh_2S_3, Rh_3S_4, and $Rh_{17}S_{15}$. Applying a new type of sulfide anion source was tried in this study to increase the composition of Rh_3S_4 in the Rh_xS_y catalyst mixture.

In the rhodium sulfide synthesis reported in the previous publications [22–25] and in the patent by De Nora [39], the source of rhodium was the $RhCl_3$ solution, and the source of sulfur was provided by the dissociation of $(NH_4)_2S_2O_3$ [25]. In this study, a new type of sulfur source, Na_2S, was used to provide the sulfide ions in the synthesis of Rh_xS_y. In the first part of the study, the new sulfur source was used to synthesize rhodium sulfide catalysts on the untreated commercial carbon substrate XC72R. Besides the different sulfur sources, the same thermal treatment temperature and ramp rates as those of the catalyst with $(NH_4)_2S_2O_3$ were used. An interesting fact that the Rh_xS_y catalyst with Na_2S as the sulfur source (purple curve with downward triangle markers) is more active than the catalyst synthesized with $(NH_4)_2S_2O_3$ can be found in the cyclic voltammogram in Figure 1. The Rh_xS_y/untreated carbon synthesized by Na_2S shows a lower overpotential for the HOR as compared to those of the Rh_xS_y/untreated carbon with $(NH_4)_2S_2O_3$ (blue curve with circle markers), indicating that the usage of Na_2S is a potential approach to increase the HOR activity of rhodium sulfide catalyst.

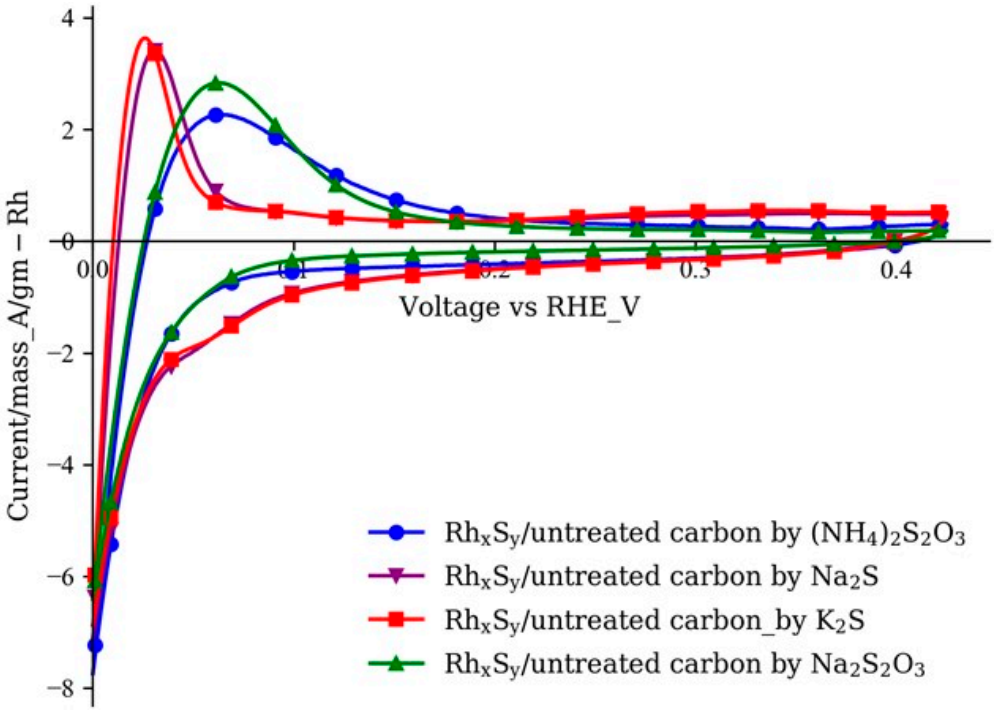

Figure 1. Cyclic voltammograms of Rh_xS_y synthesized by the sulfur sources with different cations and anions (electrolyte: 1 M N_2-saturated H_2SO_4 solution; working electrode: catalyst-coated GDE; counter electrode: Pt foil; reference electrode: saturated calomel electrode (SCE); scan rate: 10 mV/s).

The cation and anion in the synthesis solution changed when Na_2S was used instead of $(NH_4)_2S_2O_3$. To identify the sources of the improvement in activity of the catalyst, sulfide compounds with a different combination of cations and anions, K^+, Na^+, S^{2-}, and $S_2O_3^{2-}$ were used to synthesize Rh_xS_y. The influence of the type of cations to the final activity can be excluded or confirmed by introducing different cations while maintaining the same anions in the sulfide compounds. No change in the size and location of the HOR peak of the CVs was observed when the sodium ion in Na_2S (purple curve with downward triangle markers) was replaced by the potassium ion in K_2S (red curve with square markers). The same result was observed with the catalysts synthesized with $(NH_4)_2S_2O_3$ (blue curve with circle symbols) and $Na_2S_2O_3$ (green curve with upward triangle symbols). The Rh_xS_y catalysts synthesized with Na_2S and K_2S show similar HOR peak voltages that are more negative than those of the Rh_xS_y catalysts made with the thiosulfate sulfur sources. The results from these two groups indicate that the cation in the sulfur source has no effect on the rhodium sulfide catalytic performance. Rather, the HOR activity of Rh_xS_y catalysts is affected mainly by the anion source. Moreover, the more active catalysts come from the sulfur sources with the sulfide S^{2-} anions. The reason as to why the direct sulfide S^{2-} anion source led to higher HOR activity versus the indirect thiosulfate $S_2O_3^{2-}$ source will be discussed later in Figure 5.

After we confirmed that the increase in the HOR activity of the Rh_xS_y catalysts was associated with the readily available sulfide anion in the solution (when Na_2S or K_2S was used), the new sulfur source was combined with the carbon functionalization process and the diffusion-controlled nanoparticle growth process developed in our previous study to synthesize the high-active-surface-area and high-HOR-activity Rh_xS_y catalyst. From the results given in Figure 2a, the mass-specific ECSAs obtained from the HOR peak of the cyclic voltammograms of the Rh_xS_y catalyst on pretreated carbon synthesized with Na_2S (green curve with upward triangles) and $(NH_4)_2S_2O_3$ (blue curve with circles) increased more than four folds over those with untreated carbon substrates. These results show the effectiveness of the carbon functionalization and diffusion-controlled particle growth process in reducing the catalyst nanoparticle size. The slightly higher increase in the ECSA of the catalyst

synthesized with Na_2S (4.6 versus 4.0 times) can be attributed to the smaller nanoparticles (NPs) that were obtained when a slower rate was used to add the Na_2S solution to the synthesis solution. As reported in the previous work [24], the $(NH_4)_2S_2O_3$ was added in 15 equal aliquots with a 2-min interval (30 min total) while in this process the Na_2S amount was added to the synthesis solution over a duration of 2 h by a peristaltic pump. Our previous work has shown that maintaining a low concentration of Rh_2S_3 monomer in the bulk solution could lead to the diffusion-controlled nanoparticle growth condition that resulted in the more dispersed and smaller nanoparticles. Next, the results in Figure 2a also show that the HOR onset potentials and mass-specific current density peaks of the catalysts synthesized with Na_2S are shifted to a more negative potential. These characteristics suggest that these catalysts had a higher HOR specific activity, which, if it were true, would be confirmed by the polarization curves of these catalysts.

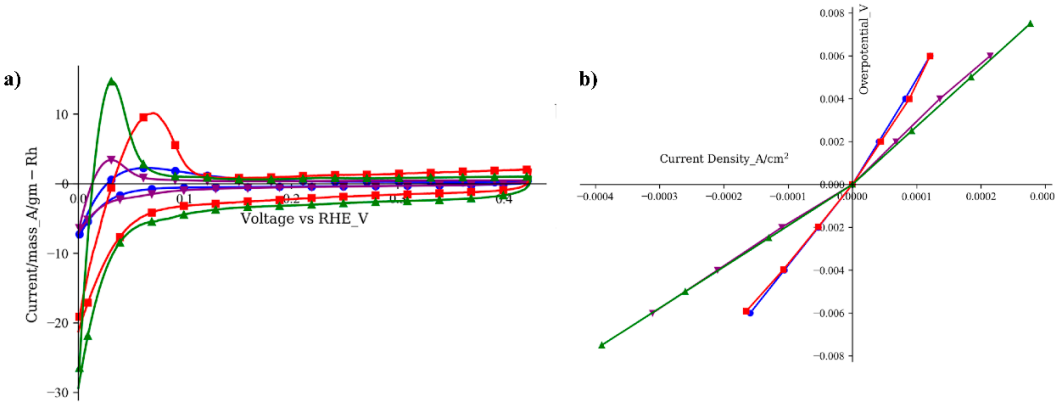

Markers	Catalyst	ECSA/mass_ m2/gm-Rh	i_o(HOR)_ A/cm2	i_o(HER)_ A/cm2	i_o^*(HOR)_ A/gm-Rh	i_o^*(HER)_ A/gm-Rh
●	Rh_xS_y/untreated carbon by $(NH_4)_2S_2O_3$	9.1	0.47	0.62	0.43	0.56
▼	Rh_xS_y/untreated carbon by Na_2S	9.3	0.56	0.81	0.52	0.76
■	Rh_xS_y/pretreated carbon by $(NH_4)_2S_2O_3$	36.5	0.46	0.64	1.68	2.32
▲	Rh_xS_y/pretreated carbon by Na_2S	43	0.58	0.82	2.49	3.51

Figure 2. (**a**) Cyclic voltammograms of rhodium sulfide synthesized with different carbon substrates and sulfur sources (electrolyte: 1 M N_2-saturated H_2SO_4 solution; working electrode: catalyst-coated GDE; counter electrode: Pt foil, reference electrode: SCE; scan rate: 10 mV/s); (**b**) linear polarization curves of rhodium sulfide catalysts synthesized with different carbon substrates and sulfur sources (electrolyte: 1 M H_2-saturated H_2SO_4 solution; rotation speed: 2400 rpm; working electrode: catalyst-coated GC-RDE; counter electrode: Pt foil; reference electrode: SCE).

The linear polarization results in Figure 2b show that the active-area-specific HOR/HER activities of the rhodium sulfide catalysts synthesized with Na_2S on the untreated/pretreated carbons are higher (i.e., lower vs. I slopes) than those of the catalysts synthesized with $(NH_4)_2S_2O_3$, validating the CV results presented in Figure 2a. Since the current density used in Figure 2b is the current per ECSA of the catalyst, the exchange current density i_o here is the ECSA-based exchange current density. By multiplying the mass-specific ECSA obtained in Figure 1, the mass-specific exchange current density i_o^* can be calculated. The HOR/HER active-area-specific activities of the Rh_xS_y catalysts made with Na_2S are 1.2 times (0.56 A/cm^2 vs. 0.47 A/cm^2) and 1.3 times (0.81 A/cm^2 vs. 0.62 A/cm^2) those of the Rh_xS_y catalysts made with $(NH_4)_2S_2O_3$ on untreated and pretreated carbon substrates, respectively. It is also worth noting that the higher activity of the Rh_xS_y catalysts obtained with Na_2S is not affected by the slow addition rate of the sulfur source solution and the types of the carbon substrate. The decrease in the NPs size by the application of functionalized carbon and the mass-transportation-controlled nanoparticle growth process using the slow sulfur source addition rate

approach is confirmed by the TEM micrographs in Figure 3. With this combined approach, the average particle size of the Rh_xS_y/pretreated carbon synthesized with $(NH_4)_2S_2O_3$ decreases to 5.2 nm, while that of the Rh_xS_y/pretreated carbon synthesized with Na_2S decreases further to 3.2 nm with a lower sulfur source addition rate.

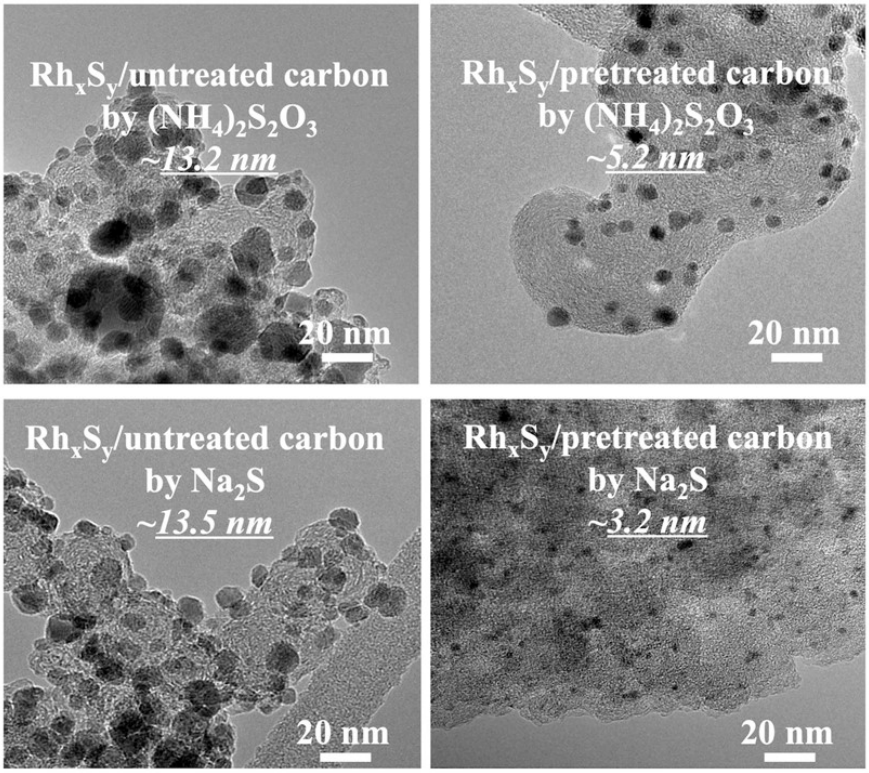

Figure 3. TEM micrographs of the Rh_xS_y catalysts synthesized on different carbon support materials and with different sulfur sources.

As in the previous discussion, the voltages of the HOR peaks of the Rh_xS_y synthesized with Na_2S and $(NH_4)_2S_2O_3$ in Figure 1 are the main observed differences. Moreover, the results in Figure 1 hinted that the change in the Rh_xS_y activity could be attributed to the type of the anion source. The smaller overpotential of the HOR in Figure 1 and the higher catalytic activity from the linear polarization results in Figure 2b confirm that the Rh_xS_y synthesized with Na_2S has a higher HOR activity. XRD and XPS were used next to explore the nature of the different activities of the Rh_xS_y synthesized with Na_2S and $(NH_4)_2S_2O_3$.

In Figure 4a,b, the XRD results show that the crystal structures of the Rh_xS_y are not modified by the use of the functionalized carbon substrate since the XRD patterns of the Rh_xS_y on the untreated carbon (blue and purple curves), and the pretreated carbon (red and green curves) are similar. The Rh_xS_y synthesized with Na_2S and $(NH_4)_2S_2O_3$ on both of the untreated and treated carbons show distinctively different characteristic XRD peaks at 36–43° and 72–75°, respectively. In the first fingerprint characteristic region (36–43°), the Rh_xS_y made from the conventional sulfur source, $(NH_4)_2S_2O_3$, has the intensity peak strength sequence as P4 > P1 > P3 > P2, while the catalyst made with Na_2S shows the intensity peak order of P1 > P4 > P3 > P2. The possible reasons for the change in the intensity order of the XRD fingerprint region may be attributed to the different crystal facets or the different crystal phases of the catalysts. The standard crystal patterns of $Rh_{17}S_{15}$ and Rh_3S_4 from ICDS also show that $Rh_{17}S_{15}$ has a peak located at around 73°, while Rh_3S_4 shows nothing. The second fingerprint region in Figure 4b shows that the catalysts synthesized with $(NH_4)_2S_2O_3$ have a stronger peak, while the catalysts synthesized with Na_2S show a weaker peak. The stronger characteristic peak at 73° may be attributed to a higher content of $Rh_{17}S_{15}$ in the Rh_xS_y made with $(NH_4)_2S_2O_3$, and the

weaker peak at 73° of the Rh_xS_y made with Na_2S may likewise be attributed to a lower $Rh_{17}S_{15}$ and higher Rh_3S_4 composition. The changes in the XRD spectra in Figure 4b suggest that there is a different crystal composition between the Rh_xS_y catalysts synthesized with $(NH_4)_2S_2O_3$ and Na_2S. However, XRD cannot detect Rh_3S_4 well because of its low crystallinity, which means that XRD is not a highly convincing characterization method to address this question [26,40].

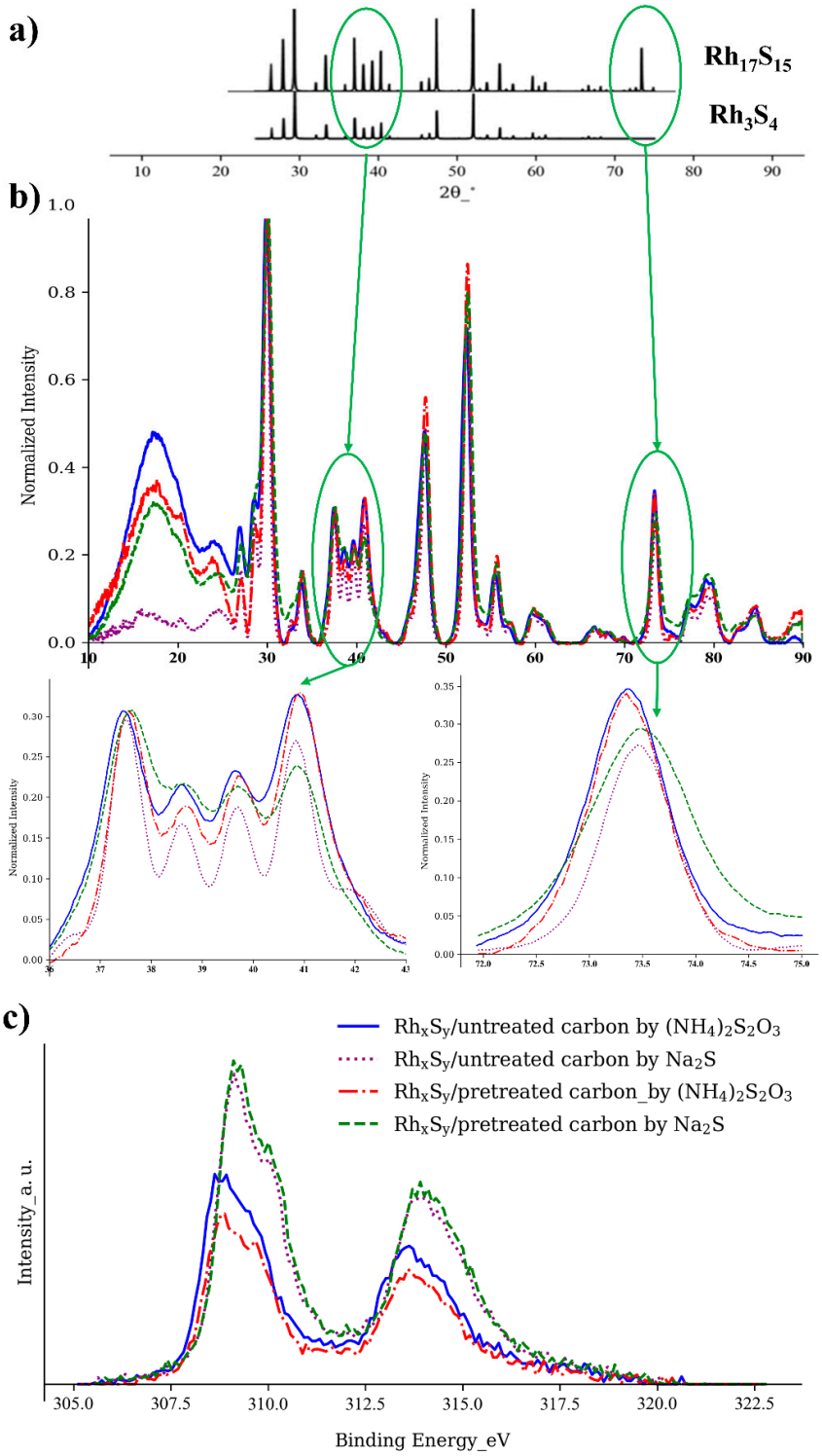

Figure 4. (**a**) Standard XRD spectra (Rh_3S_4 ICDS No. 410813, $Rh_{17}S_{15}$ ICDS No. 410838); (**b**) XRD spectra and (**c**) Rh 3d XPS of Rh_xS_y synthesized with different carbon substrates and sulfur sources.

The bonding information of Rh atoms in $Rh_{17}S_{15}$ and Rh_3S_4 measured by XPS may be a better indicator of the HOR/HER activity improvement. It is clear in Figure 4c that the binding energy of Rh atoms of the Rh_xS_y synthesized with Na_2S has a higher energy (~0.25 eV) than those of the Rh_xS_y from $(NH_4)_2S_2O_3$, indicating that these two types of Rh_xS_y catalysts may have different outer electronic structures of Rh. The electronegativity of Rh (2.28) and S (2.58) may cause a shift in the peak positions. The electrons of the bond tend to concentrate at the atom with the larger electronegativity. A more positive XPS peak indicates the Rh atoms have a lower electron density that is caused by more coordination with the neighboring sulfur atoms [42]. The space group C2/m tells that half of the rhodium atoms in the Rh_3S_4 phase are fully coordinated by the six surrounding S atoms, while three-quarters of the rhodium atoms in the $Rh_{17}S_{15}$ phase with the space group Pm3m are only coordinated with the four neighboring S atoms [29,43]. The crystal structures of the multiple crystal phases of rhodium sulfide can be found in Figure 5. Based on the crystal structures, it is inferred that the Rh_xS_y synthesized with Na_2S contains more Rh_3S_4, due to the positively shifted Rh 3d peak position (the lower electron density on Rh centers). According to the DFT calculation, the Rh_3S_4 phase is a more active catalyst for the HOR/HER [27]. Therefore, a higher percentage of the more active crystal phase Rh_3S_4 can contribute to the higher activity of the rhodium sulfide catalysts synthesized with the Na_2S.

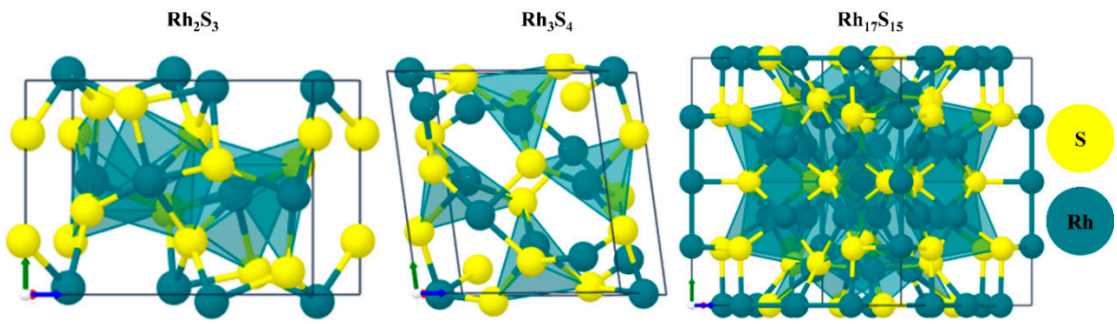

Figure 5. Crystal structures of Rh-S materials [44] (license under by CC-BY 4.0).

The different compositions of the crystal phases in the two rhodium sulfide catalysts may be explained by the mechanisms that generate the sulfide anion from $S_2O_3^{2-}$ and S^{2-}. Na_2S is a strong electrolyte that dissociates into Na^+ and S^{2-} completely and immediately, although with some hydrolysis of S^{2-}. The concentration of Na_2S used in this synthesis is 4.5 M, while the pH of the Na_2S solution was measured as 10.8. From the hydrolysis formula of S^{2-} ($S^{2-} + H_2O^- > HS^- + OH^-$), one can infer that only 0.014% S^{2-} was hydrolyzed in this process. The dominant form of sulfur in the Na_2S solution is S^{2-}. On the other hand, $(NH_4)_2S_2O_3$ releases the S^{2-} via a two-step mechanism as shown below,

$$(NH_4)_2S_2O_3 \rightarrow 2NH_4^+ + S_2O_3^{2-} \quad (2)$$

$$S_2O_3^{2-} + H_2O \rightarrow 2H^+ + SO_4^{2-} + S^{2-} \quad (3)$$

Compared to the direct dissociation of Na_2S, the two-step dissociation of $(NH_4)_2S_2O_3$ releases sulfide anion slowly. Since the dissociation of $S_2O_3^{2-}$ releases H^+, the level of $S_2O_3^{2-}$ dissociation can be determined by measuring the pH of the solution. Two H^+ cations are released per dissociated $S_2O_3^{2-}$ in the equation above. Figure 6 shows the dissociation level of $(NH_4)_2S_2O_3$ versus the temperature. The results show only 0.0025% of $S_2O_3^{2-}$ dissociated when the solution was heated from room temperature to the reaction temperature of the Rh_2S_3 precursor synthesis process (100 °C). It can be inferred from these results that the dissociation of thiosulfate in the synthesis of Rh_2S_3 is driven by the consumption of sulfide ions by the precipitation with Rh^{3+}. The equilibrium of the dissociation reaction of thiosulfate is continuously driven forward by the Rh^{3+} sulfidation reaction. In our synthesis

process, 20% excess sulfur source was used to precipitate all of the expensive precious rhodium. At the end of the precursor synthesis process, the extra $S_2O_3^{2-}$ exists mostly in the form of $S_2O_3^{2-}$ instead of S^{2-}. On the other hand, the Na_2S dissociates completely and quickly. Consequently, the extra Na_2S stays in the S^{2-} form after the complete sulfidation of Rh^{3+}. The extra S^{2-} may be either left on the precursor surface or incorporated into the amorphous Rh_2S_3 particles, due to its small size and affinity with the coordinated sulfur atoms in the precursor. Since Rh_xS_y is a type of heterogeneous catalyst which only catalyzes the reactions on the surface, the crystal phase composition on the catalyst surface determines the catalytic activity. Although most of the extra S^{2-} may be removed during the catalyst preparation, the residue of the extra S^{2-} in the particles should still be enough to modify the catalyst phases on the surface.

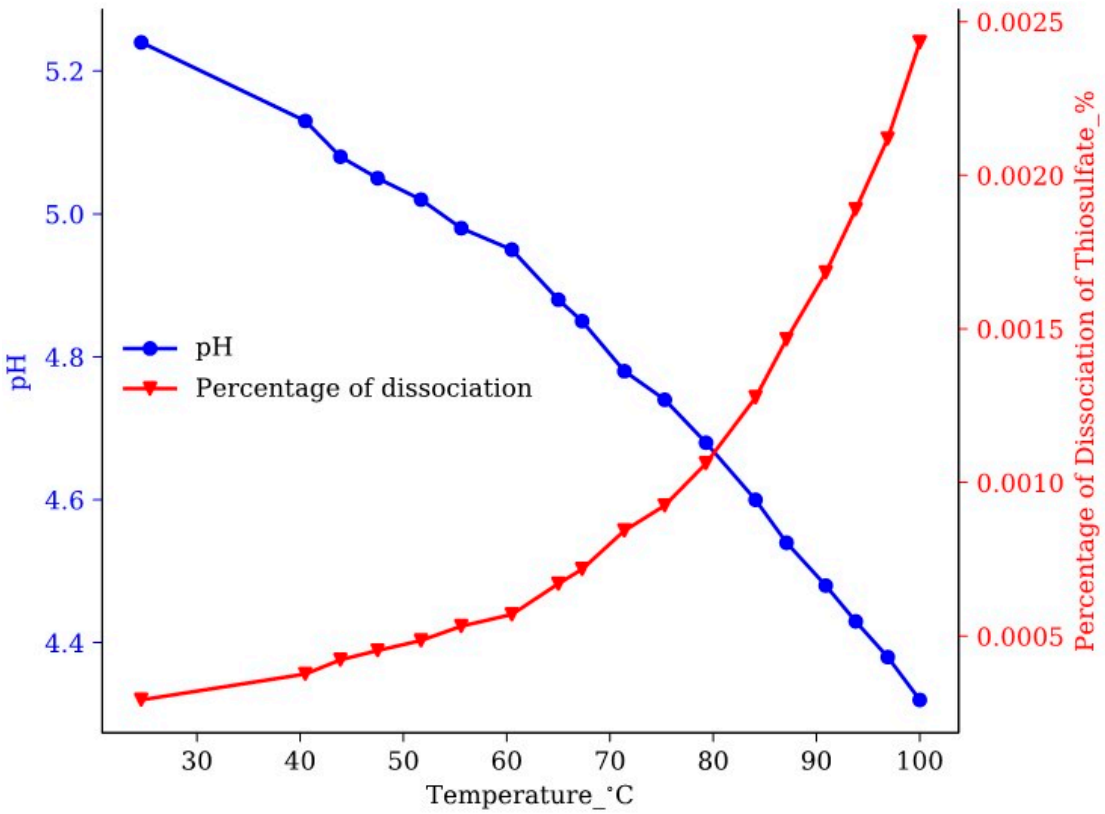

Figure 6. Dissociation of ammonium thiosulfate versus the temperature.

After the Rh_2S_3 precursor was synthesized, it was converted to the active Rh_3S_4 and $Rh_{17}S_{15}$ phases by the thermal treatment at 700 °C. The ΔG of the conversion of $Rh_{17}S_{15}$ to Rh_3S_4 is around –85 kJ/mol at 700 °C indicating that this conversion is spontaneous and can occur if extra sulfide ions are available [45]. We hypothesized that the extra S^{2-} in the particles provided by the excess Na_2S facilitated the formation of the more active crystal phase Rh_3S_4 during the thermal treatment process based on the phase diagram and the dissociation mechanisms. The results shown in Figure 7 support this hypothesis. The HOR peaks of the Rh_xS_y catalysts with 120% $(NH_4)_2S_2O_3$ and Na_2S are located at 71 mV and 43 mV, respectively. When the excess amount of Na_2S was reduced from 120% to 103%, the HOR peak voltage shifted from 43 mV to 55 mV, indicating a lower HOR activity. The lack of extra S^{2-} in the thermal treatment decreases the generation of the more active Rh_3S_4 phase and finally results in lower activity.

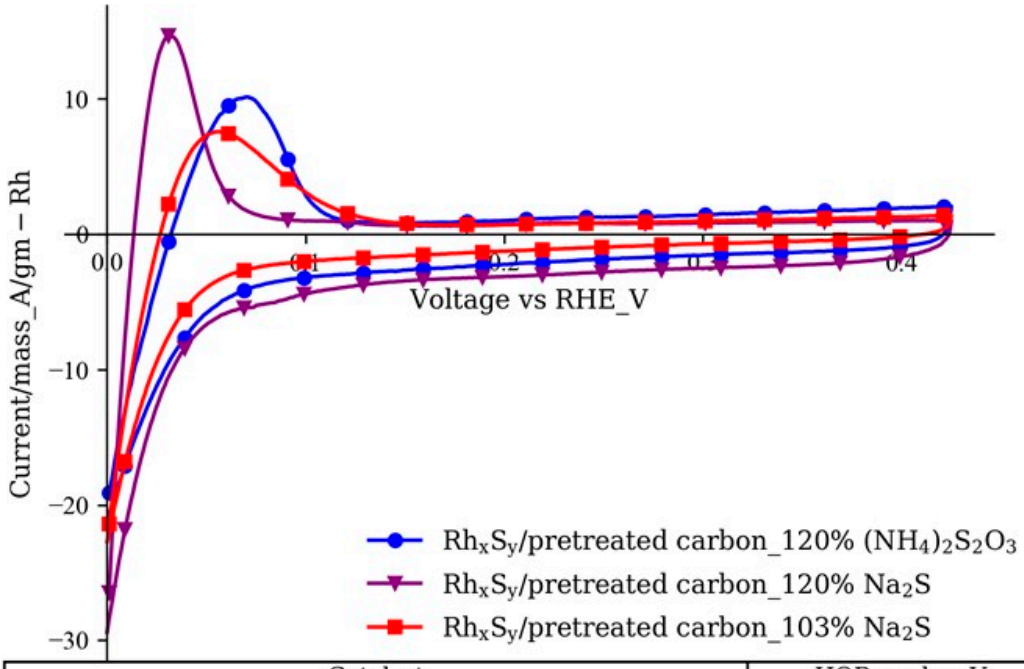

Catalyst	HOR peak_mV
Rh_xS_y/pretreated carbon_120% $(NH_4)_2S_2O_3$	71
Rh_xS_y/pretreated carbon_120% Na_2S	43
Rh_xS_y/pretreated carbon_103% Na_2S	55

Figure 7. Cyclic voltammograms of Rh_xS_y catalysts with different excess levels of sulfur sources (electrolyte: 1 M N_2-saturated H_2SO_4 solution; working electrode: catalyst-coated GDE; counter electrode: Pt foil; reference electrode: SCE; scan rate: 10 mV/s).

Once the cause for the improved activity with Na_2S was identified, the performance of the Rh_xS_y catalyst synthesized with extra Na_2S and the functionalized carbon material was tested in an H_2-Br_2 fuel cell. To achieve a better fuel cell performance, the Nafion® ionomer-unfriendly ketone groups on the carbon surface that were needed for the high dispersion and precipitation of the rhodium sulfide nanoparticles in the catalyst synthesis process have to be converted into the Nafion® ionomer-friendly carboxylic groups. As reported in the previous publications [24,25], the performance of the Rh_xS_y catalyst on the ketone-dominated carbon surface substrate decreases rapidly in the high current density region because of the high mass transport resistance created by the poor affinity of the ketone groups to the Nafion® ionomer in the catalyst ink. This poor affinity of the catalyst for the Nafion® ionomer results in a non-uniform, poorly dispersed, and thick ionomer electrolyte coating that reduces the effective electrochemical active area in the catalyst layer and highly hinders the transport of hydrogen molecules to the catalyst surface. Our previous work confirms that the Nafion®-unfriendly ketone groups on the carbon surface can be converted to the Nafion®-friendly carboxylic groups by using the Baeyer–Villiger reaction and ester hydrolysis process without any adverse effect on the precipitated catalysts [24].

Figure 8 shows the polarization curves of the hydrogen-bromine fuel cells with Rh_xS_y catalysts on the pretreated/untreated carbons synthesized by Na_2S and $(NH_4)_2S_2O_3$ and the commercial catalyst. These curves have been IR-corrected to remove the ohmic contribution from the membrane, electrolyte, and electronic components in the fuel cell. This IR correction allows only the effect of the kinetic and mass transport effects in the cell to be investigated. Note that all the pretreated carbons used here had been subjected to the surface functional conversion from the ketone group to the carboxylic group by the Baeyer–Villiger and hydrolysis reaction process. The performance of the fuel cells with the Rh_xS_y/untreated carbon synthesized by Na_2S and $(NH_4)_2S_2O_3$ is limited by their low mass-specific

electrochemical active surface area, 9.3 and 9.1 m^2/gm-Rh, respectively. With the functionalized carbon, mass-transfer-controlled nanoparticle growth process, and the surface functional conversion, the fuel cells with the Rh_xS_y on the carboxylic-dominated treated carbon synthesized with Na_2S and $(NH_4)_2S_2O_3$ show lower kinetic resistance, no mass transfer resistance created by the ketone-Nafion® ionomer repulsion [25], and much better charge and discharge performance. The Rh_xS_y catalyst with higher activity from the higher Rh_3S_4 composition and larger ECSA from the smaller nanoparticle size obtained from the optimized addition rate of the new Na_2S sulfur source outperforms all other catalysts in the fuel cell test. Its discharge performance at 200 mV below the OCV (i.e., overpotential) of the fuel cell is 1.2 times and 6.2 times higher than that of the catalyst synthesized by $(NH_4)_2S_2O_3$ on treated carbon and untreated carbon and 2.5 times better than that of the commercial catalyst from BASF. The fact that the mass-specific HOR activity of the Rh_xSy/pretreated carbon with Na_2S as the sulfur source was improved by 48% over that of the Rh_xS_y/pretreated carbon with $(NH_4)_2S_2O_3$ as the sulfur source while its fuel cell performance was only increased by 16% shows that the improvement achieved in the RDE test was not fully demonstrated in the fuel cell system test. The reason may be attributed to the fact that the Nafion®:catalyst ratio currently used in the catalyst ink was not yet optimized for this new catalyst. We suspect that a higher Nafion®:catalyst ratio may be needed to coat the higher mass-specific surface area achieved in this new catalyst. This aspect will be investigated in our future research.

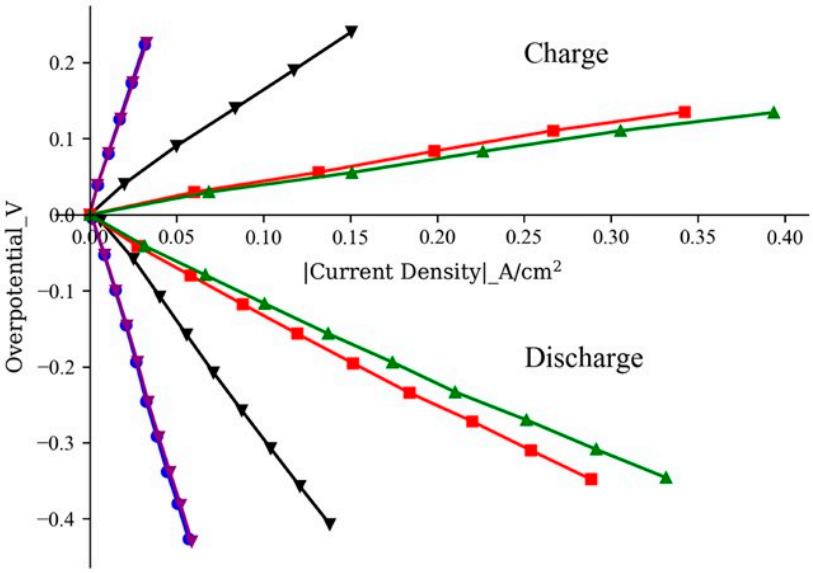

Catalyst	Rh_xS_y/untreated carbon by Na_2S	Rh_xS_y/untreated carbon by $(NH_4)_2S_2O_3$	Rh_xS_y/pretreated carbon by Na_2S	Rh_xS_y/pretreated carbon by $(NH_4)_2S_2O_3$	Rh_xS_y from BASF
Symbol	▼	●	▲	■	▼
Current density at 0.2V below OCV A/cm²	0.028	0.027	0.175	0.152	0.0712

Figure 8. Discharge and charge polarization curves of H_2-Br_2 fuel cells with different catalysts after full IR correction (weight ratio of Nafion® ionomer:catalyst = 1:1).

Finally, as explained in our previous papers, the fuel cell charge performance with rhodium sulfide catalysts, which are bifunctional catalysts, is always better than the discharge performance because the hydrogen evolution reaction occurs on both the rhodium and sulfur surface sites, while the hydrogen oxidation reaction occurs only on the rhodium surface sites. While the optimization and improvement of the discharge performance of hydrogen-bromine fuel cell have been our primary focus, any improvement that is achieved with the HOR performance during the discharge mode is expected to affect also the HER performance during the charge mode of the fuel cell.

4. Conclusions

A rhodium sulfide catalyst with high mass-specific surface area, high Nafion®-ionomer-affinity, and high HOR/HER activity was synthesized and evaluated in this study. The functionalization of the carbon support and diffusion-controlled nanoparticle growth process were used to create better catalyst distribution and smaller nanoparticle sizes (from 13.5 nm to 3.2 nm). As a result, the catalyst mass-specific electrochemical surface area increased from 9.3 to 43.0 m^2/gm-Rh, which is close to the 50 m^2/gm-Rh goal for this material. The rhodium sulfide catalyst synthesized with the new sulfur source, Na_2S, was more active than the catalyst synthesized with the previously used sulfur source, $(NH_4)_2S_2O_3$. The XPS investigation revealed that the Rh_xS_y synthesized with Na_2S contained a higher portion of the more active Rh_3S_4 phase, as determined by the DFT calculation. The higher Rh_3S_4 phase composition was attributed to the fast and complete release mechanism of S^{2-} of Na_2S that provide the extra S^{2-} in the amorphous Rh_2S_3 nanoparticles. The presence of the extra S^{2-} in the precursor material during the thermal treatment process promoted the conversion of $Rh_{17}S_{15}$ to Rh_3S_4, due to the negative ΔG of the process. The repulsion effect between the surface ketone group on the carbon substrate and the Nafion® ionomer in the catalyst ink was resolved by the Baeyer–Villiger and ester hydrolysis reaction process which converted the Nafion® ionomer-unfriendly ketone group to the Nafion® ionomer-friendly carboxylic group. With higher Nafion® affinity and better dispersion of the ionomer in the catalyst layer, the discharge performance of fuel cell with Rh_xS_y/functionalized carbon synthesized with Na_2S surpassed those of the fuel cells with Rh_xS_y on untreated and treated carbon synthesized by $(NH_4)_2S_2O_3$ and the commercial catalyst from BASF by 6.2, 1.2, and 2.4 times, respectively. With further optimization of the synthesis process, we believe the 50 m^2/gm-Rh goal could be reached.

Author Contributions: The research was done by Y.L. under the direction of T.V.N. All authors have read and agreed to the published version of the manuscript.

Funding: This research received no external funding.

Conflicts of Interest: The authors declare that the research was conducted in the absence of any commercial or financial relationships that could be construed as a potential conflict of interest.

References

1. Hosseini, S.E.; Andwari, A.M.; Wahid, M.A.; Bagheri, G. A review on green energy potentials in Iran. *Renew. Sustain. Energy Rev.* **2013**, *27*, 533–545. [CrossRef]
2. Zhou, S.; Matisoff, D.C.; Kingsley, G.A.; Brown, M.A. Understanding renewable energy policy adoption and evolution in Europe: The impact of coercion, normative emulation, competition, and learning. *Energy Res. Soc. Sci.* **2019**, *51*, 1–11. [CrossRef]
3. U.S. Energy Information Administration. *Electric Power Annual 2018*; U.S. Energy Information Administration: Washington, DC, USA, 2019.
4. Korpaas, M.; Holen, A.T.; Hildrum, R. Operation and sizing of energy storage for wind power plants in a market system. *Int. J. Electr. Power* **2003**, *25*, 599–606. [CrossRef]
5. Pettinger, K.-H.; Dong, W. When does the operation of a battery become environmentally positive? *J. Electrochem. Soc.* **2016**, *164*, A6274–A6277. [CrossRef]
6. Wang, P.; Chen, D.; Pan, J.; Zeng, X.; Sun, Y.; Lin, Y.; Shu, X.; Jin, X. Wrinkled reduced graphene oxide supported nano Ag4Bi2O5 rods as greatly enhanced catalyst for zinc-air battery. *J. Electrochem. Soc.* **2019**, *166*, A968–A974. [CrossRef]
7. Glass, W.; Boyle, G. Performance of hydrogen-bromine fuel cells. *Adv. Chem.* **1965**, *47*, 203–220. [CrossRef]
8. Kreutzer, H.; Yarlagadda, V.; Nguyen, T.V. Performance evaluation of a regenerative hydrogen-bromine fuel cell. *J. Electrochem. Soc.* **2012**, *159*, F331–F337. [CrossRef]
9. Lin, G.; Chong, P.Y.; Yarlagadda, V.; Nguyen, T.V.; Wycisk, R.J.; Pintauro, P.N.; Bates, M.; Mukerjee, S.; Tucker, M.C.; Weber, A.Z. Advanced hydrogen-bromine flow batteries with improved efficiency, durability and cost. *J. Electrochem. Soc.* **2016**, *163*, A5049–A5056. [CrossRef]

10. Cho, K.T.; Ridgway, P.; Weber, A.Z.; Haussener, S.; Battaglia, V.; Srinivasan, V. High performance hydrogen/bromine redox flow battery for grid-scale energy storage. *J. Electrochem. Soc.* **2012**, *159*, A1806–A1815. [CrossRef]
11. Livshits, V.; Ulus, A.; Peled, E. High-power H_2/Br_2 fuel cell. *Electrochem. Commun.* **2006**, *8*, 1358–1362. [CrossRef]
12. Hydrobromic Acid Price. *Alibaba*. Available online: https://www.alibaba.com/product-detail/hydrogen-bromide-hbr-CAS-10035-10_1441964535.html?spm=a2700.galleryofferlist.0.0.32365fa5qAkqTo (accessed on 1 July 2020).
13. V2O5 Vanadium Pentoxide Flake 98% Price. *Vanadiumprice*. Available online: https://www.vanadiumprice.com/ (accessed on 1 July 2020).
14. Weber, A.Z.; Nguyen, T.V. Redox flow batteries–reversible fuel cells. *J. Electrochem. Soc.* **2016**, *163*, Y1. [CrossRef]
15. Yarlagadda, V.; Dowd, R.P.; Park, J.W.; Pintauro, P.N.; Nguyen, T.V. A comprehensive study of an acid-based reversible H2-Br2 fuel cell system. *J. Electrochem. Soc.* **2015**, *162*, F919–F926. [CrossRef]
16. Yarlagadda, V.; Lin, G.; Chong, P.Y.; Nguyen, T.V. High surface area carbon electrodes for bromine reactions in H2-Br2 fuel cells. *J. Electrochem. Soc.* **2016**, *163*, A5126–A5133. [CrossRef]
17. Sharma, M.; Doan, H.; Alsudairi, A.M.; Pavlicek, R.; Lajami, A.; Miller, T.; Ghoshal, S.; Bates, M.; Jia, Q.; Halligan, K. Fundamental study of nitrogen functionalized catalyst for H2-Br2 redox flow battery systems. Meeting Abstracts. In Proceedings of the 231st Electrochemical Society Meeting, New Orleans, LA, USA, 15 April 2017. [CrossRef]
18. García, I.L.E.; Gómez, A.; de la, R.; Viramontes, N.J.P.; Torres, S.M.D.; Betancourt, M.L.G. MoS2-Pt nanoparticles deposited on carbon nanostructures by a microwave assisted method as hydrogen electrodes for H2–Br2 flow batteries. Meeting Abstracts. In Proceedings of the AiMES 2018, Cancun, Mexico, 30 September 2018–4 October 2018. [CrossRef]
19. Saadi, K.; Nanikashvili, P.; Tatus-Portnoy, Z.; Hardisty, S.; Shokhen, V.; Zysler, M.; Zitoun, D. Crossover-tolerant coated platinum catalysts in hydrogen/bromine redox flow battery. *J. Power Sources* **2019**, *422*, 84–91. [CrossRef]
20. Gershinsky, G.; Nanikashvili, P.; Elazari, R.; Zitoun, D. From the sea to hydrobromic acid: Polydopamine layer as corrosion protective layer on platinum electrocatalyst. *Acs Appl. Energy Mater.* **2018**, *1*, 4678–4685. [CrossRef]
21. Nguyen, T.V.; Kreutzer, H.; Yarlagadda, V.; McFarland, E.; Singh, N. HER/HOR catalysts for the H2-Br2 fuel cell system. *ECS Trans.* **2013**, *53*, 75–81. [CrossRef]
22. Masud, J.; Nguyen, T.V.; Singh, N.; McFarland, E.; Ikenberry, M.; Hohn, K.; Pan, C.-J.; Hwang, B.-J. A RhxSy/C catalyst for the hydrogen oxidation and hydrogen evolution reactions in HBr. *J. Electrochem. Soc.* **2015**, *162*, F455–F462. [CrossRef]
23. Li, Y.; Nguyen, T.V. Core-shell rhodium sulfide catalyst for hydrogen evolution reaction / hydrogen oxidation reaction in hydrogen-bromine reversible fuel cell. *J. Power Sources* **2018**, *382*, 152–159. [CrossRef]
24. Li, Y.; Nguyen, T.V. Synthesis and evaluation of RhxSy catalyst with high affinity for Nafion ionomer for HOR/HER in a H2-Br2 regenerative fuel cell. *J. Electrochem. Soc.* **2019**, *166*, F701–F702. [CrossRef]
25. Li, Y.; Nguyen, T.V. Synthesis and evaluation of RhxSy catalyst with functionalized carbon for HOR/HER in H2-Br2 reversible fuel cell. *J. Electrochem. Soc.* **2018**, *165*, F1139–F1146. [CrossRef]
26. Singh, N.; Hiller, J.; Metiu, H.; McFarland, E. Investigation of the electrocatalytic activity of rhodium sulfide for hydrogen evolution and hydrogen oxidation. *Electrochim. Acta* **2014**, *145*, 224–230. [CrossRef]
27. Singh, N.; Upham, D.C.; Liu, R.-F.; Burk, J.; Economou, N.; Buratto, S.; Metiu, H.; McFarland, E.W. Investigation of the active sites of rhodium sulfide for hydrogen evolution/oxidation using carbon monoxide as a probe. *Langmuir* **2014**, *30*, 5662–5668. [CrossRef] [PubMed]
28. Singh, N.; Gordon, M.; Metiu, H.; McFarland, E. Doped rhodium sulfide and thiospinels hydrogen evolution and oxidation electrocatalysts in strong acid electrolytes. *J. Appl. Electrochem.* **2016**, *46*, 497–503. [CrossRef]
29. Diéguez, O.; Marzari, N. First-principles characterization of the structure and electronic structure of α-S and Rh-S chalcogenides. *Phys. Rev. B* **2009**, *80*, 214115. [CrossRef]
30. Taylor, J.R. A Knudsen cell study of molten sulfides: Thermodynamics of the Rh-S system. *Metal. Trans. B* **1981**, *12*, 47–54. [CrossRef]

31. Li, Y.; Nguyen, T.V. Core-shell rhodium sulfide catalyst for HER/HOR in HBr solution. *ECS Trans.* **2016**, *72*, 19–26. [CrossRef]
32. Kristl, M.; Dojer, B.; Gyergyek, S.; Kristl, J. Synthesis of nickel and cobalt sulfide nanoparticles using a low cost sonochemical method. *Heliyon* **2017**, *3*, e00273. [CrossRef]
33. Gulla, A.F.; Allen, R.J. Carbon Supported Metal Sulphide Catalyst for Electrochemical Oxygen Reduction. US Patents US20080202923 A1, 28 August 2008.
34. Allen, R.J.; Gulla, A.F. Synthesis of Noble Metal, Sulphide Catalysts in A Sulfide Ion-Free Aqueous Environment. US Patents US20050164877 A1, 28 July 2005.
35. Gullá, A.F.; Gancs, L.; Allen, R.J.; Mukerjee, S. Carbon-supported low-loading rhodium sulfide electrocatalysts for oxygen depolarized cathode applications. *Appl. Catal. Gen.* **2007**, *326*, 227–235. [CrossRef]
36. Takei, C.; Kobayashi, R.; Mizushita, Y.; Hiramitsu, Y.; Kakinuma, K.; Uchida, M. Platinum anti-dissolution mechanism of Pt/Nb-SnO2 cathode catalyst layer during load cycling in the presence of oxygen for polymer electrolyte fuel cells. *J. Electrochem. Soc.* **2018**, *165*, F1300–F1311. [CrossRef]
37. Feng, T.; Xie, A.; Du, J.; Pan, F.; Chen, P.; Zhu, S.; Luo, S.; Yao, C. Glycerol oxidation over the Pt-Cerium oxide/porous polyaniline catalyst. *J. Electrochem. Soc.* **2018**, *165*, A2750–A2757. [CrossRef]
38. III, D.L.W.; Jung, S.Y.; Nguyen, T.V. Effect of direct liquid water injection and interdigitated flow field on the performance of proton exchange membrane fuel cells. *Electrochim. Acta* **1998**, *43*, 3795–3809. [CrossRef]
39. Parthé, E.; Hohnke, E.; Hulliger, F. A new structure type with octahedron pairs for Rh2S3, Rh2Se3 and Ir2S3. *Acta Crystallogr.* **1967**, *23*, 832–840. [CrossRef]
40. Beck, J.; Hilbert, T. Ein, altes' Rhodiumsulfid mit überraschender Struktur: Synthese, Kristallstruktur und elektronische Eigenschaften von Rh3S4. *Zeitschrift Für Anorganische Und Allgemeine Chemie* **2000**, *626*, 72–79. [CrossRef]
41. Tamura, M.; Kon, K.; Satsuma, A.; Shimizu, K. Volcano-curves for dehydrogenation of 2-propanol and hydrogenation of nitrobenzene by SiO2-supported metal nanoparticles catalysts as described in terms of a d-band model. *Acs Catal.* **2012**, *2*, 1904–1909. [CrossRef]
42. He, J.; He, X.; Liu, L.; Hu, B.; Bai, F.; Zhang, P.; Zhao, Y. Tailoring carbon materials substrate to modify the electronic structure of platinum for boosting its electrocatalytic activity. *J. Electrochem. Soc.* **2018**, *165*, F247–F252. [CrossRef]
43. Geller, S. The crystal structure of the superconductor Rh17S15. *Acta Crystallogr.* **1962**, *15*, 1198–1201. [CrossRef]
44. Jain, A.; Ong, S.P.; Hautier, G.; Chen, W.; Richards, W.D.; Dacek, S.; Cholia, S.; Gunter, D.; Skinner, D.; Ceder, G.; et al. The Materials Project: A materials genome approach to accelerating materials innovation. *Appl. Mater.* **2013**, *1*, 011002. [CrossRef]
45. Jacob, K.T.; Gupta, P. Gibbs free energy of formation of rhodium sulfides. *J. Chem. Thermodyn.* **2014**, *70*, 39–45. [CrossRef]

© 2020 by the authors. Licensee MDPI, Basel, Switzerland. This article is an open access article distributed under the terms and conditions of the Creative Commons Attribution (CC BY) license (http://creativecommons.org/licenses/by/4.0/).